

See discussions, stats, and author profiles for this publication at: <https://www.researchgate.net/publication/51236924>

# Simulating electron spin resonance spectra of macromolecules labeled with two dipolar-coupled nitroxide spin labels from trajectories

ARTICLE *in* PHYSICAL CHEMISTRY CHEMICAL PHYSICS · JUNE 2011

Impact Factor: 4.49 · DOI: 10.1039/c1cp20430k · Source: PubMed

---

CITATIONS

6

---

READS

12

## 2 AUTHORS:



**Deniz Sezer**

Sabanci University

15 PUBLICATIONS 478 CITATIONS

SEE PROFILE



**Snorri Th Sigurdsson**

University of Iceland

113 PUBLICATIONS 2,819 CITATIONS

SEE PROFILE

Cite this: *Phys. Chem. Chem. Phys.*, 2011, **13**, 12785–12797

www.rsc.org/pccp

PAPER

## Simulating electron spin resonance spectra of macromolecules labeled with two dipolar-coupled nitroxide spin labels from trajectories

Deniz Sezer<sup>a</sup> and Snorri Th. Sigurdsson<sup>b</sup>

Received 18th February 2011, Accepted 20th May 2011

DOI: 10.1039/c1cp20430k

An efficient method for simulating continuous-wave electron spin resonance spectra (ESR) of molecules labeled with two dipolar-coupled nitroxides from trajectories of the molecular motion is presented. Two approximate treatments of the dipolar spin evolution, resulting in significantly shorter simulation times, are examined in order to determine their range of applicability. The approach is illustrated in the context of a double-helical B-DNA. ESR spectra for DNA undergoing anisotropic global diffusion and internal stretching dynamics are calculated for three different labeling geometries with the spin labels bracketing, respectively, three, two and one base pairs. While multifrequency spectra of all three labeling schemes are very sensitive to DNA tumbling, the last one is found to be most informative about the local DNA dynamics.

### 1. Introduction

The possibility to introduce spin labels at specific positions along the polymer chains of proteins<sup>1</sup> and nucleic acids<sup>2–7</sup> has made electron spin resonance (ESR) an important experimental technique for probing the local structure and dynamics of proteins,<sup>8–10</sup> DNA,<sup>11–15</sup> and RNA.<sup>16,17</sup> Perhaps more importantly for structural biology, labeling simultaneously with two spin labels and detecting the dipolar interaction of their electron spins provide valuable long-range information. Under favorable conditions distances of up to 80 Å can be probed using pulse-ESR methods.<sup>18</sup> In the last decade, measuring long-range distances in doubly-labeled molecules using DEER (double electron–electron resonance)—also known as four-pulse PELDOR (pulse electron double resonance)—has become well established and has been widely applied to a diverse range of biological systems.<sup>18–21</sup> However, distance measurements with pulse-ESR methods are performed under cryogenic temperatures in frozen samples, which lack information about the biologically relevant molecular dynamics.

Detecting dipolar interactions between two electron spins in solution at room temperature by performing routine continuous-wave (cw) ESR experiments has been of interest ever since the early days of site-directed spin-labeling.<sup>22,23</sup> Although the range of distances accessible with cw-ESR is limited to up to ~20 Å,<sup>24</sup> valuable information has been obtained for many different biomolecules. The construction of models for the

open states of the potassium channel KcsA<sup>25,26</sup> and the mechanosensitive channel MscL<sup>27,28</sup> on the basis of information from dipolar-broadened cw-ESR spectra are two particularly notable examples.

In contrast to the pulse-ESR methods in the solid state, for which a robust quantitative analysis for extracting distances and distance distributions exists,<sup>29</sup> deducing distances from the solution cw-ESR spectra has remained very qualitative. To a large extent, the uncertainties associated with a qualitative analysis have been compensated by the extensive labeling of many sites. In this way, it has been possible to correlate the regularities in the extensive data sets with structural changes, as exemplified in ref. 25–28.

The work of Hustedt and Beth stands out as a systematic effort to develop the tools necessary to rigorously extract distances and distance distributions from cw-ESR spectra of mobile proteins.<sup>30</sup> A numerical scheme for calculating dipolar-coupled ESR spectra in the presence of rigid-body rotational diffusion has been developed for isotropic tumbling and used to test the sensitivity of such spectra to global dynamics.<sup>31</sup> More recently, to allow for disorder of the spin label side chain, and thus account for a distribution of inter-spin-label distances, the tether-in-a-cone model has been introduced and combined with the calculation of dipolar-coupled cw-ESR spectra.<sup>32</sup> The application of this model to doubly-labeled T4 lysozyme, however, was limited to rigid-limit spectra in which global or internal dynamics were absent.<sup>32</sup> It is therefore highly desirable to be able to rigorously quantify dipolar-coupled cw-ESR spectra in the presence of complex global and internal dynamics expected from spin-labeled biomolecules in solution at physiological temperatures.

Recently, we have developed efficient numerical integrators for treating the spin dynamics of an electron–nuclear spin system

<sup>a</sup> Faculty of Engineering and Natural Sciences, Sabanci University, Orhanlı-Tuzla, 34956 Istanbul, Turkey.  
E-mail: dsezer@sabanciuniv.edu;

Web: <http://myweb.sabanciuniv.edu/dsezer/>

<sup>b</sup> Science Institute, University of Iceland, Dunhaga 3, 107 Reykjavik, Iceland

characteristic of nitroxides and for simulating stochastic trajectories for the most general case of anisotropic, restricted rotational diffusion.<sup>33</sup> Propagating the rotational and spin dynamics in time allows for the separation of the quantum mechanical and classical motional aspects of the problem, resulting in a highly modular and flexible simulation approach. ESR spectra for a very broad range of complex motional models, including the familiar MOMD<sup>34</sup> and SRLS<sup>35</sup> models, could therefore be easily simulated.<sup>33</sup> In fact, it was possible to treat motions on different spatial and temporal scales by seamlessly combining phenomenological dynamics with atomistic molecular dynamics simulations.<sup>36–38</sup>

In the present paper this technology is extended to biomolecules labeled simultaneously with two dipolar-coupled nitroxide spin labels. Our goal is to make possible the efficient simulation of cw-ESR spectra of such biomolecules from stochastic models of their dynamics and, eventually, from MD trajectories. This will hopefully allow for the extensive quantitative evaluation of different dynamical models against multifrequency cw-ESR experiments performed at physiological temperatures. In this way, molecular dynamics probed by solution ESR can be properly interpreted in their structural context, thus assessing their importance for biological function.

Recently, a novel spin label that lacks internal degrees of freedom has been introduced for the labeling of nucleic acids.<sup>7,15</sup> DNA molecules labeled with two such spin labels have been synthesized and characterized by PELDOR.<sup>39,40</sup> The distances between the spin labels in these samples, however, were too large to be detected by room-temperature cw-ESR. Here, we use the developed computational methodology to assess whether two closely-placed spin labels will provide experimental access to the global and local DNA dynamics in solution by cw-ESR.

The paper is organized as follows. The treatment of the spin dynamics for two dipolar-coupled nitroxides with the purpose of simulating cw-ESR spectra is developed in the next section, where an efficient numerical integrator is presented and two approximate treatments of the dipolar interaction are considered. Section III is concerned with modeling the global and internal dynamics of the spin-labeled macromolecule. The general discussion is followed by a concrete treatment of a double-helical, B-form DNA containing two spin labels. Spectral simulations illustrating the developed formalism in applications to the introduced DNA systems are presented in Section IV. Here, in addition to exploring the sensitivity of the dipolar-coupled cw-ESR spectra to the parameters of the global and internal DNA motions, the approximate simulation strategies are compared with the exact treatment. Our conclusions are given in Section V.

## II. Spin dynamics

We consider an ensemble of nitroxide free radicals in solution. Each nitroxide spin label contains a system of two interacting spins: the spin of an unpaired electron ( $S = 1/2$ ) and a nitrogen nuclear spin ( $I = 1$  for  $^{14}\text{N}$  and  $I = 1/2$  for  $^{15}\text{N}$ ). Differently from ref. 33, where the electron-nuclear spin system on a single nitroxide was assumed not to be interacting with the spin system on another nitroxide, here the electron

spins on pairs of nitroxides are coupled through their dipolar interaction. Having in mind a biomolecule covalently labeled with two spin labels, the pair of interacting nitroxides is assumed to be fixed in time. In addition, the sample is assumed to be sufficiently dilute such that there are no inter-pair interactions. As a result, the object of interest is the two electron–two nuclear spin system on the two interacting spin labels. The state of this spin system can be described by the density operator  $\hat{\rho}$ , which is a  $36 \times 36$  (for two  $^{14}\text{N}$ ) or  $16 \times 16$  (for two  $^{15}\text{N}$ ) matrix. In the following we will make explicit reference to the naturally abundant  $^{14}\text{N}$  species. However, the presented formalism is general and applies to the  $^{15}\text{N}$  case as well.

### A. The spectrum

A typical cw-ESR spectrum recorded under weak microwave power can be calculated as the one-sided Fourier transform of the free induction decay (FID) of the transverse magnetization after a  $\pi/2$  ( $90^\circ$ ) pulse.<sup>41</sup> Because ESR is not a single-molecule technique, a large number of spins—each one experiencing different realizations of the stochastic molecular dynamics—contribute to the signal. In the simulation approach described in this work, the macroscopic transverse magnetization  $\langle M_+(t) \rangle$  is calculated by simulating the evolution of the microscopic magnetization  $M_+(t)$  associated with a single trajectory and averaging over many realizations of the motional dynamics. Instead of calculating  $M_+$ , in numerical work it is much more convenient to work in a coordinate frame that rotates about the applied constant magnetic field with the Larmor frequency of the electron spin,  $\omega_0$ . Denoting variables in the rotating frame with a prime, the magnetization can be written as

$$M'_+(t) = \text{Tr}\{\hat{S}_+ \hat{\rho}'(t)\}, \quad (1)$$

where  $\hat{\rho}(t)$  is the density operator of the spin system of interest evaluated along a single dynamical trajectory. At the end, the spectrum is calculated as

$$S(\omega - \omega_0) = \int_0^\infty \langle M'_+(t) \rangle e^{-i\omega t} dt. \quad (2)$$

For a system of dipolar-coupled electron spins on two nitroxides the transverse magnetization is given by the sum

$$\begin{aligned} M'_+(t) &= \text{Tr}\{(\hat{S}_+^1 + \hat{S}_+^2) \hat{\rho}'(t)\} \\ &= \text{Tr}\{\rho_{+\uparrow}(t) + \rho_{+\downarrow}(t) + \rho_{\uparrow+}(t) + \rho_{\downarrow+}(t)\}, \end{aligned} \quad (3)$$

where  $\hat{S}_+^1$  and  $\hat{S}_+^2$  are the spin operators of the two interacting electrons. The matrices  $\rho_{+\uparrow}$ ,  $\rho_{+\downarrow}$ ,  $\rho_{\uparrow+}$ , and  $\rho_{\downarrow+}$  are sub-blocks of the full density matrix defined as

$$\begin{aligned} \rho_{+\uparrow} &= \langle -+ | \hat{\rho}' | ++ \rangle, \quad \rho_{+\downarrow} = \langle -- | \hat{\rho}' | ++ \rangle, \\ \rho_{\uparrow+} &= \langle +- | \hat{\rho}' | ++ \rangle, \quad \rho_{\downarrow+} = \langle -- | \hat{\rho}' | +- \rangle. \end{aligned} \quad (4)$$

In the context of the full density matrix written in the two-electron-spin basis

$$|m_S^1, m_S^2\rangle = \{|++\rangle, |+-\rangle, |-+\rangle, |--\rangle\}, \quad (5)$$

these sub-blocks are positioned as follows:

$$\hat{\rho}' = \begin{bmatrix} - & - & - & - \\ \rho_{\uparrow+} & - & - & - \\ \rho_{+\uparrow} & - & - & - \\ - & \rho_{+\downarrow} & \rho_{\downarrow+} & - \end{bmatrix}. \quad (6)$$

The trace on the second line in eqn (3) is only over the nuclear spin states of the first and second nitroxides. To calculate the spectrum, therefore, we need to be able to propagate numerically these four  $9 \times 9$  (for  $I = 1$ ) matrices starting from their initial values. For all the four matrices, the initial condition appropriate for the description of an FID after a  $\pi/2$  pulse is the outer product of the  $3 \times 3$  identity matrices in the respective nuclear Hilbert spaces, which is the  $9 \times 9$  identity matrix.

Below we deduce how to numerically propagate the matrices (4) starting from the evolution of the full density matrix. It turns out that in the high-field approximation their evolution is decoupled from the evolution of the other sub-blocks of  $\hat{\rho}'$ .

## B. The spin Hamiltonian

The spin Hamiltonian of the interacting nitroxides is

$$\hat{H}(t) = \hat{H}^1(t) + \hat{H}^2(t) + \hat{H}^D(t), \quad (7)$$

where (in units of angular frequency)

$$\hat{H}^\alpha(t) = |\gamma_e|[\mathbf{B} \cdot \mathbf{G}^\alpha(t) \cdot \hat{\mathbf{S}}^\alpha + \hat{\mathbf{I}}^\alpha \cdot \mathbf{A}^\alpha(t) \cdot \hat{\mathbf{S}}^\alpha] - \gamma_n \mathbf{B} \cdot \hat{\mathbf{I}}^\alpha \quad (8)$$

and

$$\hat{H}^D(t) = \hat{\mathbf{S}}^1 \cdot \mathbf{D}(t) \cdot \hat{\mathbf{S}}^2 + J \hat{\mathbf{S}}^1 \cdot \hat{\mathbf{S}}^2. \quad (9)$$

The first two terms on the right-hand side of eqn (7) correspond to each of the two spin labels designated by  $\alpha = 1, 2$ . They account for the electron and nuclear Zeeman interactions as well as the hyperfine interaction on each nitroxide [eqn (8)]. The third term couples the electron spins on the two spin labels through their dipolar and scalar interactions [eqn (9)]. In eqn (8),  $\gamma_e$  and  $\gamma_n$  are, respectively, the electronic and nuclear gyromagnetic ratios,  $\hat{\mathbf{S}}^\alpha$  is the spin operator of the unpaired electron on radical  $\alpha$ , and  $\hat{\mathbf{I}}^\alpha$  is the spin operator of the nitrogen nucleus on radical  $\alpha$ . Similarly,  $\mathbf{G}^\alpha$  and  $\mathbf{A}^\alpha$  are the Zeeman and hyperfine coupling tensors of spin label  $\alpha$ . In eqn (8),  $\mathbf{A}^\alpha$  is in units of magnetic field while  $\mathbf{G}^\alpha$  is obtained as the ratio of the dimensionless electron  $g$ -tensor  $\mathbf{g}^\alpha$ , which is typically reported, and the free electron  $g$ -factor  $g_e$ :  $\mathbf{G}^\alpha \equiv \mathbf{g}^\alpha/g_e$ . Commonly, the magnetic tensors  $\mathbf{G}^\alpha$  and  $\mathbf{A}^\alpha$  are taken to be diagonal in the same nitroxide-fixed coordinate frame  $\mathbf{N}^\alpha$ . Their explicit time dependence in eqn (8) is due to the dynamics of this frame with respect to the stationary laboratory frame  $\mathbf{L}$ , in which the constant magnetic field  $\mathbf{B} = (0, 0, B_0)$  is applied. Since the spins are quantized along  $\mathbf{B}$  all the vector and tensor components in the Hamiltonian are with respect to  $\mathbf{L}$ . Following the standard practice, the nuclear quadrupolar (for  $I = 1$ ) interaction has been neglected. The nuclear Zeeman interaction, which is also typically neglected in simulations of slow-motional cw-ESR spectra, is retained in the expressions of this section. However, it is set to zero in the illustrative simulations of Section IV.

Being interested in two nitroxides, we assume that the Zeeman tensors for the two spin systems are identical.

Neglecting their anisotropy, and invoking the point dipole approximation, the dipolar coupling tensor in eqn (9) is given by

$$\mathbf{D}(t) = \frac{\mu_0 \hbar}{4\pi} \gamma_e^2 \frac{\mathbf{E} - 3\mathbf{r}(t)\mathbf{r}(t)}{r^3(t)}, \quad (10)$$

where  $r(t)$  is the magnitude and  $\mathbf{r}(t)$  the direction of the vector  $\mathbf{r}(t)$ , pointing from one of the unpaired electrons to the other, and  $\mathbf{E}$  is the  $3 \times 3$  identity matrix. The scalar coupling  $J$  in eqn (9) is invariant upon rotation of the molecules and does not depend on time.

Let us define the electron Larmor frequency  $\omega_0 = -\gamma_e B_0 G_0$ , where  $G_0 = \text{Tr}\{\mathbf{G}^\alpha\}/3$  is assumed to be the same for  $\alpha = 1, 2$ . Similarly,  $\omega_n = -\gamma_n B_0$  is taken to be the same for both spin labels. Going to the interaction picture defined by the static Hamiltonian  $\hat{H}_0 = \omega_0(\hat{S}_z^1 + \hat{S}_z^2)$  and neglecting the nonsecular terms, the  $\hat{H}^\alpha$ s become

$$\hat{H}^{\alpha'}(t) = |\gamma_e| [B_0 G_{zz}^{\alpha'}(t) + \mathbf{a}^\alpha(t) \cdot \hat{\mathbf{I}}^\alpha] \hat{S}_z^\alpha + \omega_n \hat{I}_z^\alpha. \quad (11)$$

Here,  $G_{zz}^{\alpha'}$  is the respective component (in the lab frame) of the traceless tensor  $\mathbf{G}' \equiv \mathbf{G} - G_0 \mathbf{E}$ , and the components of the vector  $\mathbf{a}$  are related to the components (in the lab frame) of the hyperfine tensor  $\mathbf{A}$ :<sup>33</sup>

$$a_i(t) = A_{iz}(t), \quad i = x, y, z. \quad (12)$$

For later convenience, we define the operator

$$\hat{V}^\alpha(t) \equiv |\gamma_e| [B_0 G_{zz}^{\alpha'}(t) + \mathbf{a}^\alpha(t) \cdot \hat{\mathbf{I}}^\alpha] / 2. \quad (13)$$

Neglecting the nonsecular terms proportional to  $\hat{S}_\pm$  in the high-field approximation is based on the assumption that the magnetic tensors  $\mathbf{G}(t)$  and  $\mathbf{A}(t)$  fluctuate on a time scale much slower than the Larmor precession time scale. Similarly, assuming that the dipolar coupling interaction varies on a much slower time scale compared to the Larmor precession of the electron spin, the high-field dipolar-scalar Hamiltonian in the rotating frame becomes

$$\begin{aligned} \hat{H}^{D'}(t) = & D(t) [\hat{S}_z^1 \hat{S}_z^2 - (\hat{S}_+^1 \hat{S}_-^2 + \hat{S}_-^1 \hat{S}_+^2) / 4] \\ & + J [\hat{S}_z^1 \hat{S}_z^2 + (\hat{S}_+^1 \hat{S}_-^2 + \hat{S}_-^1 \hat{S}_+^2) / 2] \end{aligned} \quad (14)$$

where

$$D(t) \equiv D_{zz}(t) = \frac{\mu_0 \hbar}{4\pi} \gamma_e^2 \frac{1 - 3\bar{r}_z^2(t)}{r^3(t)} \quad (15)$$

is the only matrix element of the dipolar coupling tensor  $\mathbf{D}$  that needs to be calculated. Here,  $\bar{r}_z$  is the  $z$  component of the unit vector  $\mathbf{r}$  with respect to the laboratory-fixed system of axes.

The absence of nonsecular terms automatically excludes the possibility to account for processes that lead to  $T_1$  relaxation (and thus for  $T_1$  contribution to  $T_2$ ) using the high-field Hamiltonian. When dealing with slow motional cw-ESR spectra this approximate form is typically justified since  $T_1$ , which depends on motions at the time scale of the Larmor precession, is much longer than  $T_2$ , which is dominated by slow motions.

## C. Numerical propagation of the spin dynamics

Let

$$e^{i\hbar[\hat{H}^{1'}(t) + \hat{H}^{2'}(t)]} = e^{i\hbar\hat{H}^{1'}(t)} e^{i\hbar\hat{H}^{2'}(t)} \equiv U_h^1(t) U_h^2(t) \quad (16)$$

and

$$U_h^D(t) \equiv e^{-i\hbar\hat{H}^D(t)} \quad (17)$$

denote the propagators at time  $t$  over a short time step  $h$  under the action of only the Zeeman–hyperfine interactions [eqn (16)] or the dipolar–scalar interactions [eqn (17)]. The order of  $U_h^1$  and  $U_h^2$  on the right-hand side of eqn (16) can of course be exchanged since  $\hat{H}^1$  and  $\hat{H}^2$  commute. The dipolar Hamiltonian  $\hat{H}^D$ , however, does not commute with  $\hat{H}^1$  and  $\hat{H}^2$ . For a short time step, the propagation of the density matrix under the full Hamiltonian may be performed as

$$\hat{\rho}'(t+h) = \bar{U}_h^1 \bar{U}_h^2 U_h^D \hat{\rho}'(t) \bar{U}_h^D U_h^1 U_h^2 \quad (18)$$

where  $\bar{U}$  denotes the Hermitian conjugate of  $U$  and the dependence of the propagators on  $t$  has been dropped for clarity. This scheme, correct to first order in  $h$ , implies a two-step procedure for the numerical integration in which the dipolar–scalar propagator acts first, followed by the propagator due to the Zeeman and hyperfine interactions:

$$\begin{aligned} \text{(i)} \quad \bar{\rho} &= U_h^D(t) \hat{\rho}'(t) \bar{U}_h^D(t), \\ \text{(ii)} \quad \hat{\rho}'(t+h) &= \bar{U}_h^1(t) \bar{U}_h^2(t) \bar{\rho} U_h^2(t) U_h^1(t). \end{aligned} \quad (19)$$

We now turn to the implementation details of these two steps.

**1. Short-time dipolar–scalar propagator.** We write the matrix representation of the Hamiltonian  $\hat{H}^{D'}$  in the two-electron-spin basis (5) and keep in mind that each one of the four kets  $|m_S^1, m_S^2\rangle$  has nine components in the Hilbert space of the nuclear spins, corresponding to  $(m_I^1, m_I^2) = \{11, 10, 1\bar{1}, 01, 00, 0\bar{1}, \bar{1}1, \bar{1}0, \bar{1}\bar{1}\}$ . However, this dependence will not be shown explicitly since the dipolar–scalar evolution does not mix the nuclear spin states.

The matrix representation of the dipolar–scalar Hamiltonian (14) in the basis (5) is

$$\hat{H}^{D'} = \frac{1}{4} \begin{bmatrix} D+J & 0 & 0 & 0 \\ 0 & -D-J & -D+2J & 0 \\ 0 & -D+2J & -D-J & 0 \\ 0 & 0 & 0 & D+J \end{bmatrix}. \quad (20)$$

Therefore, the matrix representation of the propagator (17) is

$$U_h^D = \begin{bmatrix} e^{-i\phi_+} & 0 & 0 & 0 \\ 0 & e^{i\phi_+} \cos \phi_- & ie^{i\phi_+} \sin \phi_- & 0 \\ 0 & ie^{i\phi_+} \sin \phi_- & e^{i\phi_+} \cos \phi_- & 0 \\ 0 & 0 & 0 & e^{-i\phi_+} \end{bmatrix} \quad (21)$$

where

$$\phi_+(t) \equiv h[D(t) + J]/4, \quad \phi_-(t) \equiv h[D(t) - 2J]/4. \quad (22)$$

Note that in the absence of scalar coupling, *i.e.*,  $J = 0$ ,  $\phi_+ = \phi_-$ . (This is the situation we consider in the numerical examples of Section IV.) For small  $\phi_-$ ,  $U_h^D$  is essentially diagonal. (The short-time dipolar propagator of the weak-coupling approximation in Section IID1 is equivalent to  $U_h^D$  from eqn (21) after setting  $\phi_- = 0$ .)

Acting with the matrix representation of  $U_h^D$  on the representation of the density matrix, eqn (6), we find that the propagation step (i) in eqn (19) is achieved as follows:

$$\begin{bmatrix} \tilde{\rho}_{+\uparrow} \\ \tilde{\rho}_{\uparrow+} \end{bmatrix} = e^{i2\phi_+} \begin{bmatrix} \cos \phi_- & i \sin \phi_- \\ i \sin \phi_- & \cos \phi_- \end{bmatrix} \begin{bmatrix} \rho_{+\uparrow}(t) \\ \rho_{\uparrow+}(t) \end{bmatrix} \quad (23)$$

and

$$\begin{bmatrix} \tilde{\rho}_{+\downarrow} \\ \tilde{\rho}_{\downarrow+} \end{bmatrix} = e^{-i2\phi_+} \begin{bmatrix} \cos \phi_- & -i \sin \phi_- \\ -i \sin \phi_- & \cos \phi_- \end{bmatrix} \begin{bmatrix} \rho_{+\downarrow}(t) \\ \rho_{\downarrow+}(t) \end{bmatrix}. \quad (24)$$

Clearly, the evolution of  $\rho_{+\downarrow}$  and  $\rho_{\downarrow+}$  is decoupled from the evolution of  $\rho_{+\uparrow}$  and  $\rho_{\uparrow+}$ . Since each one of the four density matrices in eqn (23) and (24) is a  $9 \times 9$  matrix in the nuclear Hilbert space, these short-time propagation rules should be applied 81 times—one for each of the respective nuclear-state components.

**2. Short-time Zeeman–hyperfine propagator.** The Zeeman and hyperfine interactions are limited to one or the other of the nitroxides in the pair of spin labels. Therefore, we first derive the numerical propagation rules for the density matrix  $\hat{\rho}^\alpha$  of a spin system consisting of a single electron spin and a single nuclear spin under the action of the spin Hamiltonian  $\hat{H}^\alpha$ . For  $S = 1/2$  this density matrix (in the rotating frame) can be written as

$$\hat{\rho}^{\alpha'} = \rho_{\uparrow}^\alpha \hat{S}_{\uparrow} + \rho_{\downarrow}^\alpha \hat{S}_{\downarrow} + \rho_{+}^\alpha \hat{S}_{+} + \rho_{-}^\alpha \hat{S}_{-} = \begin{bmatrix} \rho_{\uparrow}^\alpha & \rho_{-}^\alpha \\ \rho_{\downarrow}^\alpha & \rho_{+}^\alpha \end{bmatrix}, \quad (25)$$

where the electron spin operators  $\hat{S}_\kappa$  have been written in the basis  $m_S^\alpha = (+, -)$ . The “coefficients”  $\rho_\kappa^\alpha$  are  $3 \times 3$  ( $I = 1$ ) or  $2 \times 2$  ( $I = 1/2$ ) matrices in the Hilbert space of the nuclear spin. Substituting eqn (25) in the Liouville–von Neumann equation

$$\dot{\hat{\rho}}^{\alpha'}(t) = -i[\hat{H}^{\alpha'}(t), \hat{\rho}^{\alpha'}(t)], \quad (26)$$

and using the Hamiltonian (11), yields the following decoupled evolution equations for  $\rho_\kappa^\alpha$ :

$$\begin{aligned} \dot{\rho}_1^\alpha(t) &= -i[\hat{V}^\alpha(t), \rho_1^\alpha(t)] - i\omega_n[\hat{I}_z^\alpha, \rho_1^\alpha(t)] \\ \dot{\rho}_\pm^\alpha(t) &= i[\hat{V}^\alpha(t), \rho_\pm^\alpha(t)] - i\omega_n[\hat{I}_z^\alpha, \rho_\pm^\alpha(t)] \\ \dot{\rho}_\pm^\alpha(t) &= \pm i\{\hat{V}^\alpha(t), \rho_\pm^\alpha(t)\} - i\omega_n[\hat{I}_z^\alpha, \rho_\pm^\alpha(t)]. \end{aligned} \quad (27)$$

(In these expressions dot indicates a time derivative,  $[\cdot, \cdot]$  is a commutator, and  $\{\cdot, \cdot\}$  is an anticommutator.) To propagate  $\rho_\kappa^\alpha(t)$  over a short time step  $h$  we introduce the phase factors

$$\phi_B^\alpha(t) \equiv h|\gamma_e|B_0 G_{zz}^{\alpha'}(t) \quad (28)$$

and the operators

$$U_\pm^\alpha(t) \equiv e^{i h [|\gamma_e| \alpha^\alpha(t) \cdot \hat{I}^\alpha / 2 \pm \omega_n \hat{I}_z^\alpha]}. \quad (29)$$

When the nuclear Zeeman interaction is negligible,  $U_\pm^\alpha = U^\alpha$ . (In all the numerical examples of Section IV the nuclear Zeeman interaction will be neglected.) In terms of  $U_\pm^\alpha$  and  $\phi_B^\alpha$ , the short-time evolution corresponding to eqn (27) can be achieved as

$$\begin{aligned} \rho_{\uparrow}^\alpha(t+h) &= \bar{U}_+^\alpha(t) \rho_{\uparrow}^\alpha(t) U_+^\alpha(t), \\ \rho_{\downarrow}^\alpha(t+h) &= U_-^\alpha(t) \rho_{\downarrow}^\alpha(t) \bar{U}_-^\alpha(t), \\ \rho_\pm^\alpha(t+h) &= e^{\pm i \phi_B^\alpha(t)} U_\mp^\alpha(t) \rho_\pm^\alpha(t) U_\pm^\alpha(t). \end{aligned} \quad (30)$$

This integration scheme is equivalent to eqn (27) to first order in  $h$ .



It is now straightforward to deduce from eqn (30) that the second step in eqn (19) implies the updating schemes

$$\rho_{+\uparrow}(t+h) = e^{i\phi_B^1(t)} U_-^1(t) \bar{U}_+^2(t) \tilde{\rho}_{+\uparrow} U_+^2(t) U_+^1(t), \quad (31)$$

$$\rho_{\uparrow+}(t+h) = e^{i\phi_B^2(t)} \bar{U}_+^1(t) U_-^2(t) \tilde{\rho}_{\uparrow+} U_+^2(t) U_+^1(t),$$

and

$$\rho_{+\downarrow}(t+h) = e^{i\phi_B^1(t)} U_-^1(t) U_-^2(t) \tilde{\rho}_{+\downarrow} \bar{U}_-^2(t) U_+^1(t), \quad (32)$$

$$\rho_{\downarrow+}(t+h) = e^{i\phi_B^2(t)} U_-^1(t) U_-^2(t) \tilde{\rho}_{\downarrow+} U_+^2(t) \bar{U}_-^1(t).$$

According to eqn (31) and (32), the propagation of a single density matrix block requires first the action of  $U_\pm^2$  on nine (for the nuclear spin states of the unaffected nitroxide 1)  $3 \times 3$  sub-matrices, and then the action of  $U_\pm^1$  on another nine (for the nuclear spin states of the unaffected nitroxide 2)  $3 \times 3$  sub-matrices. As a result, only this part of the propagation is already at least  $72 [= 4 \times (9 + 9)]$  times slower than the propagation of the density matrix for a single nitroxide.

The two approximations considered next reduce substantially the number of operations per integration time step leading to significant speed-up. The trick is to always remain in the Hilbert spaces of the separate spin labels and avoid working in the much larger space of their outer product.

#### D. Simplifying approximations

**1. Weak dipolar coupling.** The approximation of weak dipolar coupling consists of retaining only the diagonal part, proportional to  $S_z^1 S_z^2$ , of the dipolar coupling Hamiltonian in eqn (14). Neglecting the off-diagonal part is equivalent to setting  $\phi_- = 0$  in the dipolar short-time propagator from eqn (21), which leads to a diagonal  $U_h^D$  as well. As a result, step (i) in eqn (19), previously given by eqn (23) and (24), boils down to simple multiplication by scalar phase factors:

$$\begin{aligned} \tilde{\rho}_{+\uparrow} &\approx e^{i2\phi_+(t)} \rho_{+\uparrow}(t), \quad \tilde{\rho}_{\uparrow+} \approx e^{i2\phi_+(t)} \rho_{\uparrow+}(t), \\ \tilde{\rho}_{+\downarrow} &\approx e^{-i2\phi_+(t)} \rho_{+\downarrow}(t), \quad \tilde{\rho}_{\downarrow+} \approx e^{-i2\phi_+(t)} \rho_{\downarrow+}(t). \end{aligned} \quad (33)$$

The evolution of each of the four sub-blocks of the density matrix has thus decoupled from the others, simplifying the dipolar propagation substantially. In fact, steps (i) and (ii) in eqn (19) can now be combined in a single step. The combined update for  $\rho_{+\uparrow}$ , for example, is achieved as [cf. eqn (31)]

$$\rho_{+\uparrow}(t+h) = e^{i2\phi_+(t)} e^{i\phi_B^1(t)} U_-^1(t) \bar{U}_+^2(t) \rho_{+\uparrow}(t) U_+^2(t) U_+^1(t). \quad (34)$$

Similar expressions hold for  $\rho_{\uparrow+}$ ,  $\rho_{+\downarrow}$ , and  $\rho_{\downarrow+}$ . We now make two important observations that follow directly from this much simpler evolution. For concreteness, the approximations are introduced below for  $\rho_{+\uparrow}$  but apply as well to  $\rho_{\uparrow+}$ ,  $\rho_{+\downarrow}$ , and  $\rho_{\downarrow+}$ .

Imagine that at some instant in time  $\rho_{+\uparrow}$  is proportional to the outer product of two matrices in the nuclear Hilbert spaces of the first and second nitroxides, respectively, *i.e.*, it has the following separable form

$$\rho_{+\uparrow}(t) = e^{i\theta(t)} \rho_+^1(t) \otimes \rho_\uparrow^2(t) \quad (35)$$

Then, under the weak dipolar coupling approximation,  $\rho_{+\uparrow}$  retains its separable form during later times. This can be seen by substituting eqn (35) in (34) and rewriting the result as

$$\rho_{+\uparrow}(t+h) = e^{i\theta(t+h)} \rho_+^1(t+h) \otimes \rho_\uparrow^2(t+h) \quad (36)$$

where the matrices  $\rho_+^1$  and  $\rho_\uparrow^2$  evolve only with the Zeeman and hyperfine interactions [cf. eqn (30)]:

$$\rho_+^1(t+h) = e^{i\phi_B^1(t)} U_-^1(t) \rho_+^1(t) U_+^1(t), \quad \rho_\uparrow^2(t+h) = \bar{U}_+^2(t) \rho_\uparrow^2(t) U_+^2(t), \quad (37)$$

and the premultiplying phase factor takes care of the evolution due to the dipolar coupling:

$$\delta_D(t+h) \equiv e^{i\theta(t+h)} = e^{i2\phi_+(t)} e^{i\theta(t)} = e^{i2\phi_+(t)} \delta_D(t). \quad (38)$$

In fact, at  $t = 0$  the matrix  $\rho_{+\uparrow}$ , which is the  $9 \times 9$  identity matrix, does have the postulated separable form:

$$\rho_{+\uparrow}(0) = E_9 = E_3^1 \otimes E_3^2 = \rho_+^1(0) \otimes \rho_\uparrow^2(0). \quad (39)$$

In general, the dipolar coupling destroys this form during evolution and for any  $t > 0$ ,  $\rho_{+\uparrow}(t)$  can no longer be written as an outer product. However, as we just saw, under the approximation of weak dipolar coupling  $\rho_{+\uparrow}$  remains separable.

The initial condition (39) brings us to the second important observation. Note that the numerical propagation of  $\rho_\uparrow^2$  is achieved by sandwiching it with  $\bar{U}_+^2$  and  $U_+^2$  [eqn (37)]. Since  $U_+^2$  is unitary,  $\bar{U}_+^2$  is its inverse. The initial  $\rho_\uparrow^2(0)$ , therefore, will remain identical to  $E_3$  throughout. In contrast,  $\rho_+^1$ , which also starts as  $E_3$ , will evolve in a nontrivial way under the action of  $U_-^1$  and  $U_+^1$ . Hence, we conclude that for all  $t$

$$\rho_{+\uparrow}(t) = \delta_D(t) \rho_+^1(t) \otimes E_3^2. \quad (40)$$

The implication is that the scalar  $\delta_D$  and the  $3 \times 3$  matrix  $\rho_+^1$  have all the information contained in the  $9 \times 9$  matrix  $\rho_{+\uparrow}$ . Following the same logic we deduce that

$$\rho_{\uparrow+}(t) = \delta_D(t) E_3^1 \otimes \rho_\uparrow^2(t). \quad (41)$$

Similar expressions can be obtained for  $\rho_{+\downarrow}$  and  $\rho_{\downarrow+}$  but with  $\delta_D$  replaced by its complex conjugate:

$$\rho_{+\downarrow}(t) = \delta_D^*(t) \rho_+^1(t) \otimes E_3^2, \quad \rho_{\downarrow+}(t) = \delta_D^*(t) E_3^1 \otimes \rho_\uparrow^2(t). \quad (42)$$

Substituting in eqn (3) we obtain

$$M_+(t) = \text{Re}\{\delta_D(t)\} [\text{Tr}\{\rho_+^1(t)\} + \text{Tr}\{\rho_\uparrow^2(t)\}] \quad (43)$$

for the transverse magnetization in the weak-coupling limit.

Hence, in the weak-coupling approximation only two  $3 \times 3$  matrices and a single scalar need to be evolved according to the third line in eqn (30) and eqn (38), starting from  $\rho_+^1(0) = \rho_\uparrow^2(0) = E_3$  and  $\delta_D(0) = 1$ . This should be contrasted with the general case, which required the evolution of four  $9 \times 9$  matrices. The ensuing substantial speed-up makes the approximation of weak dipolar coupling very attractive from a computational standpoint.

**2. Beyond the weak-coupling approximation.** Here, we propose and test an approximation based on imposing the structure of eqn (40)–(42) on the density matrices for all times. In contrast to the discussion above, the full (nondiagonal) dipolar–scalar Hamiltonian is used in the short-time propagation step.

Inserting  $\rho_{+\uparrow}$  and  $\rho_{\uparrow+}$  from eqn (40) and (41) into eqn (23) in order to account for the short-time evolution due to dipolar coupling spoils their desired separable forms. To recover separability, we introduce the projection operators  $\Omega^2$  and  $\Omega^1$  that act on the  $9 \times 9$  matrices  $\rho_{\kappa\mu}$  to produce the  $3 \times 3$  matrices  $\rho_{\kappa}^1 = \Omega^2 \rho_{\kappa\mu}$  and  $\rho_{\mu}^2 = \Omega^1 \rho_{\kappa\mu}$  in the separate nuclear Hilbert spaces. In terms of the matrix elements, the action of  $\Omega^2$  on  $\rho_{+\uparrow}$  is defined as<sup>42</sup>

$$\langle i | (\Omega^2 \rho_{+\uparrow}) | j \rangle = \langle i | \rho_{+\uparrow}^1 | j \rangle = \frac{1}{3} \sum_k \langle ik | \rho_{+\uparrow} | jk \rangle. \quad (44)$$

Similarly, the action of  $\Omega^1$  on  $\rho_{\uparrow+}$  produces

$$\langle k | \rho_{\uparrow+}^2 | l \rangle = \frac{1}{3} \sum_i \langle ik | \rho_{\uparrow+} | il \rangle. \quad (45)$$

Acting with  $\Omega^2$  and  $\Omega^1$  on the resulting equations, the dipolar evolution step of eqn (23) becomes

$$\begin{aligned} \langle i | \tilde{\rho}_{+\uparrow}^1 | j \rangle &= \cos \phi_- \langle i | \rho_{+\uparrow}^1 | j \rangle + i \sin \phi_- \delta_{ij} \sigma_{+}^2, \\ \langle k | \tilde{\rho}_{\uparrow+}^2 | l \rangle &= \cos \phi_- \langle k | \rho_{\uparrow+}^2 | l \rangle + i \sin \phi_- \sigma_{+}^1 \delta_{kl}, \end{aligned} \quad (46)$$

where we have defined the scalars

$$\sigma_{\kappa}^{\alpha} \equiv \frac{1}{3} \sum_i \langle i | \rho_{\kappa}^{\alpha} | i \rangle, \quad (47)$$

and used  $\langle i | E_3 | j \rangle = \delta_{ij}$ ,  $\sum_i \langle i | E_3 | i \rangle / 3 = 1$ . Updating the two  $3 \times 3$  matrices  $\tilde{\rho}_{+\uparrow}^{\alpha}$  according to the third line in eqn (30) completes the numerical propagation of the matrices  $\rho_{+\uparrow}^1$  and  $\rho_{\uparrow+}^2$ . Similarly, substituting eqn (42) in eqn (24) and projecting to the separate nuclear Hilbert spaces lead to the following evolution equations:

$$\begin{aligned} \langle i | \tilde{\rho}_{+\uparrow}^1 | j \rangle &= \cos \phi_- \langle i | \rho_{+\uparrow}^1 | j \rangle - i \sin \phi_- \delta_{ij} \sigma_{+}^2, \\ \langle k | \tilde{\rho}_{\uparrow+}^2 | l \rangle &= \cos \phi_- \langle k | \rho_{\uparrow+}^2 | l \rangle - i \sin \phi_- \sigma_{+}^1 \delta_{kl}. \end{aligned} \quad (48)$$

As before, the evolution of  $\rho_{+\uparrow}^{\alpha}$  over a time step  $h$  is completed by updating the matrices  $\tilde{\rho}_{+\uparrow}^{\alpha}$  according to eqn (30).

The projection operation performed after every step of dipolar-scalar evolution ensures that we always remain in the separate nuclear Hilbert spaces of the two coupled radicals without ever having to go to the much larger space of their outer products. However, notice that the derived approximate evolution rules for  $\rho_{+\uparrow}^{\alpha}$  in eqn (46) and (48) are distinct. Therefore, it is necessary to evolve two separate copies of  $\rho_{+\uparrow}^{\alpha}$ , one to be used in eqn (46) and the other in eqn (48). As a result, four  $3 \times 3$  matrices need to be evolved in the proposed approximation, as opposed to four  $9 \times 9$  matrices in the exact case and two  $3 \times 3$  matrices in the approximation of weak dipolar coupling.

### III. Models of molecular motion

In applications of solution ESR to biological molecules, the main interest is in deducing structural and dynamical information about the biomolecule. From that perspective, the spin dynamics considered in great detail in the previous section is of interest only to the extent that it is coupled to the molecular dynamics. Therefore, a realistic modeling of the structure and dynamics of the spin-labeled molecule is as essential for the

analysis and simulation of cw-ESR as the rigorous treatment of the spin dynamics. Our main motivation in developing a spectral simulation approach utilizing trajectories of the molecular motion lies in our desire to employ realistic molecular models—spanning the range from atomically-detailed molecular dynamics simulations to phenomenological stochastic models—in the interpretation of ESR data.

In this section, after introducing a general framework for treating global and internal molecular motions for the purposes of simulating ESR spectra, we focus on a double-helical DNA labeled with two spin labels that lack internal degrees of freedom.

#### A. Rotational transformations and a motional model

For our purposes, the coupling of the quantum to the classical dynamics is through the three rotation matrices  $R^{\text{LN}^1}$ ,  $R^{\text{LN}^2}$  and  $R^{\text{LM}}$ , describing the orientation of the systems of coordinate axes attached to the two nitroxides ( $\text{N}^1$ ) and to the macromolecule ( $\text{M}$ ) with respect to the laboratory-fixed axes ( $\text{L}$ ). Once available at every time step, these matrices are used to evaluate the following tensor components with respect to the lab frame:

$$\begin{aligned} G_{zz}^{\alpha, \text{L}}(t) &= \sum_k R_{zk}^{\text{LN}^{\alpha}}(t) G_{kk}^{\alpha, \text{N}^{\alpha}} R_{zk}^{\text{LN}^{\alpha}}(t), \\ a_i^{\alpha, \text{L}}(t) &= A_{iz}^{\alpha, \text{L}}(t) = \sum_k R_{ik}^{\text{LN}^{\alpha}}(t) A_{kk}^{\alpha, \text{N}^{\alpha}} R_{zk}^{\text{LN}^{\alpha}}(t), \end{aligned} \quad (49)$$

and

$$r_z^{\text{L}}(t) = \sum_k R_{zk}^{\text{LM}}(t) r_k^{\text{M}}(t). \quad (50)$$

The scalars  $G_{zz}^{\alpha, \text{L}}$ ,  $a_i^{\alpha, \text{L}}$  and  $r_z^{\text{L}}$  are then used to calculate the contributions of the Zeeman, hyperfine and dipolar couplings to the spin Hamiltonian. In the last equation it is assumed that the components of the inter-spin-label vector  $\mathbf{r}$  are available in a system of coordinate axes  $\text{M}$  rigidly attached to the spin-labeled molecule.

To a good approximation in most nitroxides the spin density is partitioned almost equally between the nitroxide oxygen ( $\text{O}$ ) and nitrogen ( $\text{N}$ ) atoms. This results in four relevant inter-nitroxide vectors  $\mathbf{r}$  (corresponding to the distances  $\text{O}^1\text{--O}^2$ ,  $\text{N}^1\text{--N}^2$ ,  $\text{O}^1\text{--N}^2$ ,  $\text{N}^2\text{--O}^1$ ) that need to be transformed from the molecular to the laboratory frame using eqn (50). Using these four vectors, a single dipolar tensor can be obtained as the average of the four different dipolar-coupling contributions calculated according to eqn (15). Although for large separations of the two spin labels the differences between the four vectors may be insignificant, keeping track of all four is expected to be important for a pair of close labels. (We have done so in the simulations reported in Section IV.)

A general model to follow the dynamics of the various coordinate frames with respect to each other, appropriate for a macromolecule labeled with two spin labels, can be represented as shown in Fig. 1. In this scheme, the orientation of the global molecular frame  $\text{M}$  with respect to  $\text{L}$  is assumed to undergo free diffusion (tumbling) independently from the internal dynamics of the molecule and the two spin labels. Clearly, this is an approximation, which can fail if, for

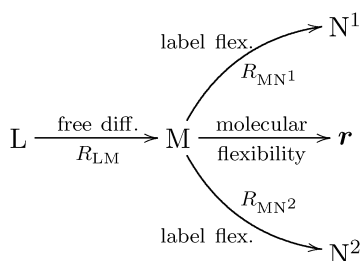


**Fig. 1** A motional model for a flexible macromolecule (M) labeled simultaneously with two spin labels ( $N^{1,2}$ ) and tumbling freely in solution. The vector  $r$ , pointing from one of the unpaired electrons to the other, as well as the orientations of the frames  $N^z$  with respect to M are affected by the internal molecular dynamics.

example, the hydrodynamic properties (*i.e.*, the rotational diffusion tensor) of the macromolecule change as a result of its internal flexibility. In principle, the trajectory-based formalism can be easily adapted to treat a time-dependent diffusion tensor if such a tensor can be estimated on the fly from the instantaneous molecular conformations. Here, we do not consider this complication and assume that the tumbling of M in solution is well described by a constant, possibly anisotropic, diffusion tensor.

The model still requires some choices to be made regarding the dynamics of the frames  $N^z$  and the vector  $r$  with respect to M. These motions, determined by the flexibility of the biomolecule and the spin labels, are most likely coupled in a non-trivial way. Therefore, we do not aim to propose a universal motional model for the internal molecular dynamics. In fact, we believe that such a model has to be developed on a case-by-case basis. Below, we adapt the general model shown in Fig. 1 to a double-stranded, B-DNA labeled with two rigid spin labels.

## B. Doubly-labeled DNA geometries

The DNA geometry that is considered is shown in Fig. 2. This choice is based on the spin-labeled DNA samples synthesized in the lab of Sigurdsson<sup>7,15</sup> and studied extensively using PELDOR by Prisner and coworkers.<sup>39,40</sup> The figure shows an ideal B-DNA with two simultaneously present spin labels. Denoting the position of the spin label on top by 1 and counting the number of base pairs going down show that the other spin label is at position 5. This labeling is therefore referred to as DNA(1,5), following the nomenclature in ref. 40. The spin–spin distances in ref. 39 and 40 were intended to be measured by PELDOR; therefore the spin labels were placed at distances larger than 20 Å starting from DNA(1,5) and going all the way to DNA(1,14). In contrast, we are interested in assessing the effect of dipolar coupling at room temperature in cw-ESR spectra, hence we look at labeling that places the spin labels in closer proximity.

The DNA(1,3) and DNA(1,4) geometries are shown in Fig. 3 for an ideal, double-helical B-DNA. Although four spin labels are shown at the same time, the two pairs are intended to be present one at a time. In the (1,3) labeling each of the two spin labels is placed on a different DNA strand such that there is a single base pair separating them. In the (1,4) labeling the spin labels are again on different strands but there are two base

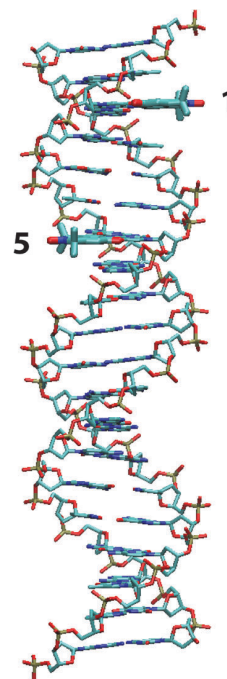


**Fig. 2** A view of the double-helical B-DNA showing the elongated shape of the molecule and the relative disposition of the two spin labels at positions 1 and 5 labeling two different strands.

pairs between them. In the case of DNA(1,5), the two spin labels bracket three base pairs, as is clearly visible in Fig. 2.

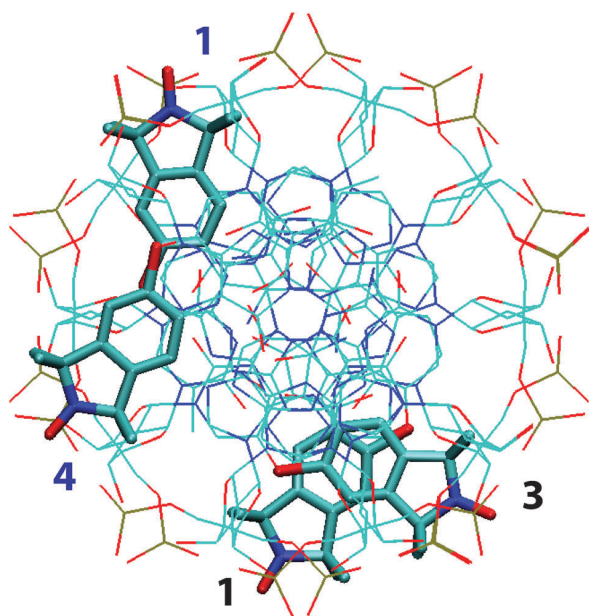
By convention, the  $z$  axes of the magnetic tensors (frames  $N^z$ ) are chosen to be perpendicular to the rings of the nitroxides. For the DNA molecules, we choose the  $z$  axis of M to be along the helix axis. As evident from Fig. 2 and 3, the spin labels are attached to the DNA such that the  $z$  axes of  $N^1$  and  $N^2$  are aligned with the  $z$  axis of M. (The deviations are about  $5^\circ$  for the models shown.) In contrast to the preserved alignment of the  $z$  axes, the relative orientation of the two frames  $N^1$  and  $N^2$  changes when going from DNA(1,3) to DNA(1,4) and DNA(1,5).

Table 1 shows the distances between the nitrogen (N) and oxygen (O) atoms of the two spin labels for the three labeling schemes that we consider in this paper. As discussed above, all the four distances are used to calculate the dipolar coupling for a given pair of spin labels. (In fact, what is used are the four different vectors  $r$  and not only the magnitudes  $|r|$  reported in Table 1.) As expected, going from DNA(1,3) to DNA(1,4) and DNA(1,5) results in larger separation between the two labels. Interestingly, for all the three geometries, the separation between the two electrons in the transverse plane is almost equal to the vertical separation, as reflected by the fact that the ratio presented in the last column of Table 1 is very close to 1.

## C. DNA tumbling and stretching dynamics

To a first approximation, in the spectral simulations of Section IV, we neglect the internal flexibility of the spin labels and the DNA molecule, and consider only the tumbling of the latter. For the model shown in Fig. 1 this corresponds to keeping  $R_{MN^1}$ ,  $R_{MN^2}$  and the components of the vectors  $r$  with respect to M fixed in time while changing  $R_{LM}$  stochastically. On the





**Fig. 3** Geometry of the (1,3) (black) and (1,4) (blue) pairs of spin labels on an ideal double-helical B-DNA. The two partners in a pair are on different strands. The view is down the helix axis. Only the atoms on the spin label which are not part of the cytosine atoms are highlighted.

**Table 1** The O–O, N–N, N–O, and O–N distances (Å) between the two spin labels and their average calculated from the molecular model of the indicated labeling scheme. The last column shows the ratio of the components of the average unit vector  $\mathbf{r}(\mathbf{r}_\perp^2 = r_x^2 + r_y^2)$  and  $\sigma_z$  (Å) is the width of the Gaussian distribution of  $r_z$  used to model DNA stretching

| Labeling | O–O  | N–N  | O–N  | N–O  | Avg. | $\sigma_z$ | $r_\perp : r_z$ |
|----------|------|------|------|------|------|------------|-----------------|
| (1,3)    | 10.8 | 9.46 | 10.1 | 10.1 | 10.1 | 2.0        | 0.71 : 0.71     |
| (1,4)    | 16.6 | 14.9 | 15.8 | 15.8 | 15.8 | 3.2        | 0.75 : 0.67     |
| (1,5)    | 22.2 | 20.1 | 21.1 | 21.1 | 21.1 | 4.2        | 0.72 : 0.70     |

basis of physical expectation that rotation about the helix axis of the 20 base-pair DNA seen in Fig. 2 is much faster than rotation about the other two axes perpendicular to the helix axis, in Section IV we choose an axial diffusion tensor with  $D_{zz} > D_{xx} = D_{yy}$  to model the DNA tumbling in solution.

The prescription that we follow to generate random trajectories of  $R_{LM}$  corresponding to free, anisotropic rotational diffusion was presented elsewhere.<sup>33</sup> For details, the reader should consult this reference. Here we only mention that trajectories are initiated from ‘freN’ points corresponding to different initial orientations of the frames M and L. Rather than being randomly chosen, the starting orientations are generated such that they cover the surface of a sphere as homogeneously as possible.<sup>43</sup>

Any internal DNA dynamics renders the transformation matrices  $R_{MN}$  and the vectors  $\mathbf{r}$  time dependent. In Section IV, we examine the effect that longitudinal DNA stretching has on the cw-ESR spectra of DNA(1,3) and DNA(1,4). The model that we use to account for DNA stretching dynamics is extremely simplified. It consists of changing the  $r_z$  components of the inter-spin-label vectors  $\mathbf{r}$  in a stochastic fashion, while

**Table 2** Parameters used in the simulation of the X- and W-band spectra in Fig. 4–8. The components of the diagonal diffusion tensor are in units of  $10^6 \text{ s}^{-1}$

| $B_0/T$ | $D_{xx}, D_{yy}, D_{zz}$ | $h/\text{ns}$ | stpN | freN | rstN | $b_L/G$ |
|---------|--------------------------|---------------|------|------|------|---------|
| 0.3485  | 10, 10, 40               | 1.0           | 300  | 6400 | 16   | 0.6     |
| 3.4     | 10, 10, 40               | 0.45          | 200  | 6400 | 64   | 1.2     |

keeping the other two components as well as the orientations of the magnetic tensors with respect to the DNA frame M unchanged. Clearly, any twisting of the DNA due to its stretching—to be reflected by the additional modulation of the orientation of the magnetic frames  $N^x$  with respect to M—is not accounted for. Similarly, no attempt has been made to model DNA bending.

In the numerical implementation of the stretching dynamics we assume that  $r_z$  undergoes diffusive motion in the harmonic potential  $u(r_z) = k(r_z - \bar{r}_z)^2/2$ , which has been normalized by the thermal energy scale. As a result,  $r_z$  is Gaussian-distributed around  $\bar{r}_z$  with probability distribution proportional to  $\exp[-(r_z - \bar{r}_z)^2/(2\sigma_z^2)]$ , where  $\sigma_z^2 = 1/k$ . The values  $\bar{r}_z$  are determined from the structural models in Fig. 2 and 3. In the simulations of Section IVC we use the  $\sigma_z$  values given in Table 1, which are chosen to be about 20% of the average distance between the two spin labels.

At the beginning of each stochastic trajectory, the starting values of  $r_z$  are randomly chosen from the Gaussian distribution specified above. For a finite time step  $h$ , increments of  $r_z$  are generated according to

$$\Delta r_z = -\frac{D_z h}{\sigma_z^2}(r_z - \bar{r}_z) + \sqrt{2D_z h} \mathcal{E}, \quad (51)$$

where  $\mathcal{E}$  is a Gaussian random variable with zero mean and unit standard deviation. In addition to reproducing the correct equilibrium probability distribution, eqn (51) also introduces relaxation dynamics on a range of time scales determined by the stretching diffusion constant  $D_z$ . The slowest relaxation time scale is equal to  $\sigma_z^2/D_z$ . For the choice of  $D_z = 1 \text{ Å}^2 \text{ ns}^{-1}$  and the values of  $\sigma_z$  from Table 1, the slowest relaxation time scales for DNA(1,3) and DNA(1,4) are 4 and 10 ns, respectively. Decreasing the diffusion rate to  $D_z = 0.25 \text{ Å}^2 \text{ ns}^{-1}$  slows down the stretching dynamics by a factor of four.

A total of ‘rstN’ different initial  $r_z$  values are drawn, each one starting a new independent trajectory. When combined with the different starting conditions for the tumbling, this leads to  $\text{freN} \times \text{rstN}$  trajectories generated in total for the simulation of a single spectrum. Each trajectory is propagated for ‘stpN’ integration steps (see Table 2). A single step spans  $h$  units of time.

## IV. Illustrative spectral simulations

All the spectra reported in this section were simulated using the following magnetic tensors

$$\begin{aligned} \mathbf{g}^N &= \text{diag}(2.0078, 2.0058, 2.0022), \\ \mathbf{A}^N &= \text{diag}(6.2, 6.2, 35.6) \text{ Gauss}. \end{aligned} \quad (52)$$

These values, typical for nitroxides, should not be taken as definitive since there has not been a systematic effort to

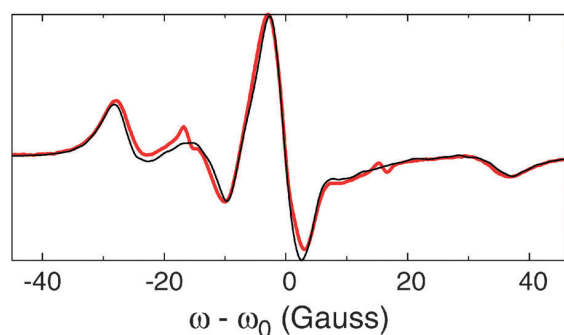


**Fig. 4** Experimental (thick red) and simulated (thin black) spectra for DNA(1,5) at  $B_0 = 0.3485$  T. The DNA was assumed to be rigid and tumble with an anisotropic diffusion tensor.

determine them unambiguously. Only  $A_{zz}$  was changed manually to match the width of the experimental spectrum shown in Fig. 4.

Details about the exact calculation of the spectrum from the simulated decay of the transverse magnetization can be found elsewhere.<sup>33</sup> Suffice it to say that Lorentzian spectral broadening, to be denoted by  $b_L$  when given in units of magnetic field, was included to mimic additional relaxation effects not related to the molecular motion (*cf.* Table 2).

#### A. Anisotropic tumbling of a rigid DNA

To make sure that the magnetic tensors and the global diffusion tensor employed in the spectral simulations are plausible, in Fig. 4 we compare the room-temperature X-band spectrum of DNA(1,5)—the only experimental spectrum presently available—with a spectrum simulated using the parameters in the first row of Table 2. The sharp features in the experimental spectrum at about  $\pm 16$  G presumably reflect the presence of free spin label in solution. Naturally, these are not captured by the simulated spectrum. Otherwise, the two spectra are seen to be in surprisingly good agreement, which is sufficient for the illustrative purposes of the present paper.

Certainly, any systematic characterization of the magnetic and motional parameters—not attempted here—will require complementary spectral information from frozen samples and measurements at higher magnetic fields. (The utility of the high-field measurements to nail down the motional parameters will become clear below.) Therefore, the values of the Zeeman and hyperfine tensors (52) as well as the diffusion tensor in Table 2 should not be taken as definitive. As we will see shortly, the single experimental spectrum shown in Fig. 4 is not sufficient to uniquely determine the components of the diffusion tensor. Nevertheless, the experiment serves as a reference point for gauging the changes in the spectra that result from changing the parameters of the motional model and including dipolar interaction.

Having gained confidence that the magnetic and motional parameters, although not definitive, are at least representative of the system at hand, we proceed with the main interest of the present work: assessing the potential of probing global and local DNA dynamics through cw-ESR spectra of DNA(1,4) and DNA(1,3) samples.

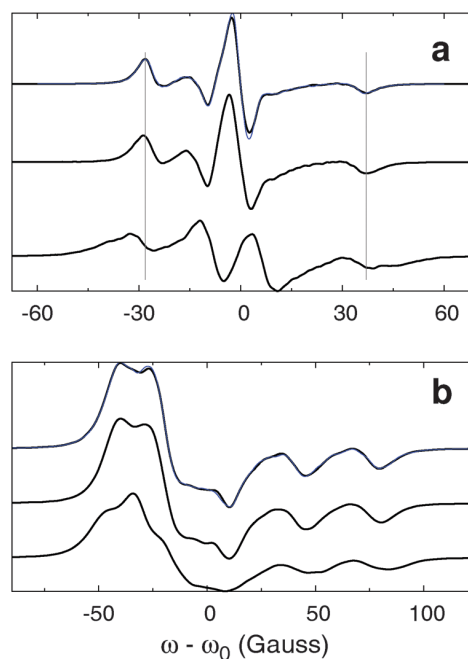


**Fig. 5** Simulated spectra at (a)  $B_0 = 0.3485$  T and (b)  $B_0 = 3.4$  T for DNA(1,5) (top), DNA(1,4) (middle), and DNA(1,3) (bottom). The spectra are shifted in the vertical direction for visual purposes. The spectra (thin blue lines) superimposed on the DNA(1,5) spectra at the X- and W-band correspond to simulations with a single nitroxide.

To this end, X- and W-band cw-ESR spectra for rigid DNA(1,5), DNA(1,4) and DNA(1,3) freely tumbling in solution were simulated (see Fig. 5). Going from DNA(1,5) to DNA(1,4) the average distance between the two unpaired electrons decreases from  $\sim 21$  Å to  $\sim 16$  Å (Table 1). The resulting changes in the X- and W-band spectra, although not dramatic, are sufficient to differentiate between the two cases. Since the average electron–electron distance goes down to  $\sim 10$  Å for DNA(1,3), both the X- and W-band spectra are drastically different from the spectra of DNA(1,4) and DNA(1,5). We may therefore expect that the DNA(1,3) system will be most effective in reporting differences in the local DNA dynamics.

To examine whether the DNA(1,5) spectra reflect the presence of dipolar coupling at all, in Fig. 5 we have superimposed them with spectra of a single nitroxide simulated using exactly the same simulation parameters. The central line in the X-band spectrum of the single spin label is seen to be slightly narrower, revealing the additional broadening in the spectrum of DNA(1,5) due to the dipolar interaction of the two labels. Since the spectral lines of the W-band spectrum are much broader, the effect of dipolar coupling is invisible at this magnetic field. Therefore, any structural or dynamical information that could potentially be reported exclusively by the dipolar coupling should be sought in the spectra of DNA(1,4) and especially DNA(1,3).

A feeling for the increased computational demands in going from a single to two coupled nitroxides can be obtained by comparing the simulation times for the spectra of a single nitroxide and DNA(1,5) shown in Fig. 5. The X- and W-band

spectra of the former were simulated in 2 min 26 s and 6 min 27 s, respectively, whereas the latter were simulated in 2 h 23 min and 6 h 22 min on a single 2.2 GHz CPU. Clearly, working in the larger dimensional Hilbert space of four spins is computationally much more demanding.

The sensitivity of the cw-ESR spectra to the global diffusion tensor is studied in Fig. 6 and 7. The spectral changes associated with diffusion around the helix axis (component  $D_{zz}$ ) are illustrated in Fig. 6, where the isotropic diffusion tensor  $D = \text{diag}(10,10,10) \times 10^6 \text{ s}^{-1}$  was employed. The X-band spectra are seen to be essentially insensitive to the imposed four-fold change in  $D_{zz}$  from 40 to 10 (Fig. 6a). From that perspective, as already alluded to, the choice  $D_{zz} = 40 \times 10^6 \text{ s}^{-1}$  to compare with the experimental spectrum in Fig. 4 is largely arbitrary. We might as well have taken an isotropic diffusion tensor. However, the extended cylindrical shape of the B-DNA argues against isotropic diffusion. In contrast, the simulated spectra in Fig. 6b demonstrate that measurements at the W-band are very sensitive to changes in  $D_{zz}$  and should be used in order to determine this component unambiguously.

In Fig. 7 we examine the sensitivity of the spectra to the length of the DNA helix. Reducing the number of base pairs in the B-DNA helix is expected to lead to faster diffusion about the axes perpendicular to the helix axis, resulting in larger  $D_{xx} = D_{yy}$  values. Thus, the spectra in Fig. 7 simulated using  $D = \text{diag}(25,25,40) \times 10^6 \text{ s}^{-1}$  correspond to a shorter helix. The extreme sensitivity of X-band measurements to this mode of transverse diffusion is clearly visible in Fig. 7a. Thus, X-band spectra are good reporter of the length of the B-DNA helix. Although the changes in the W-band spectra

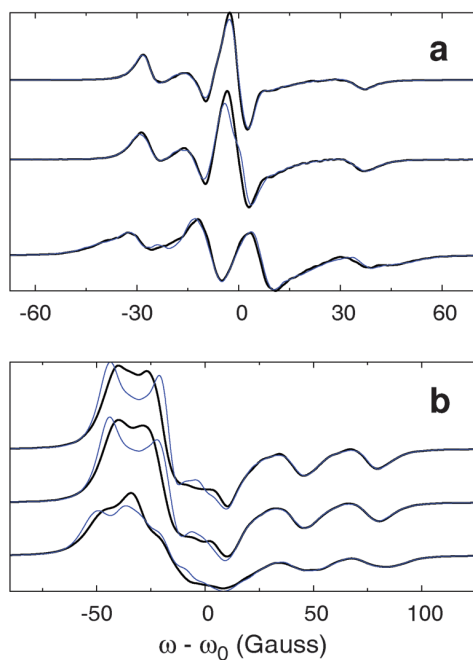


**Fig. 6** Simulated (a) X-band and (b) W-band spectra for isotropic tumbling with a diffusion tensor of  $D = \text{diag}(10,10,10) \times 10^6 \text{ s}^{-1}$  (thin blue) superimposed on the anisotropic spectra (thick black) in Fig. 5.

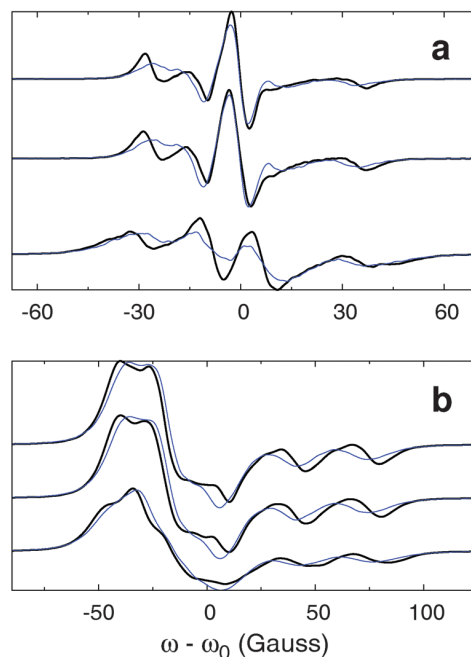


**Fig. 7** Same as Fig. 6 for a shorter B-DNA with an anisotropic diffusion tensor of  $D = \text{diag}(25,25,40) \times 10^6 \text{ s}^{-1}$ .

in Fig. 7b are less pronounced than the changes seen in Fig. 6b, if available, such high-field measurements clearly provide additional constraints on the values of  $D_{xx} = D_{yy}$ .

Taken together, the presented spectral simulations of the rigid DNA systems undergoing anisotropic tumbling show that a comparative multifrequency study of DNA(1,5), DNA(1,4) and DNA(1,3) samples is expected to be very informative about the rigid-body DNA dynamics in solution.

## B. Testing the approximate spectral simulations

The approximation of weak dipolar coupling is routinely used in the quantitative analysis of DEER (PELDOR) time traces, where it is completely justified.<sup>18,29</sup> However, its range of validity has to be ensured before it is used to simulate cw-ESR spectra. Here we test this approximation together with the alternative approximation from Section IID2, in which the separable forms of the density matrices were imposed [cf. eqn (40)–(42)].

In Fig. 8, the approximate X- and W-band spectra simulated using the parameters in Table 2 are compared with the exact simulations from Fig. 5. Both approximations show very good agreement with the X- and W-band spectra of DNA(1,5). For this labeling geometry, however, the effect of dipolar coupling is negligibly small to begin with, as was already demonstrated. Hence, the good performance of the tested approximations for DNA(1,5) is not very informative.

At the X-band the weak-coupling approximation starts failing already for DNA(1,4) producing narrower spectral lines as a result of insufficient mixing of the nuclear spin states. Its performance is miserable for DNA(1,3). The approximation of separable matrices does a consistently better job—it is extremely good for DNA(1,4) but fails as well for

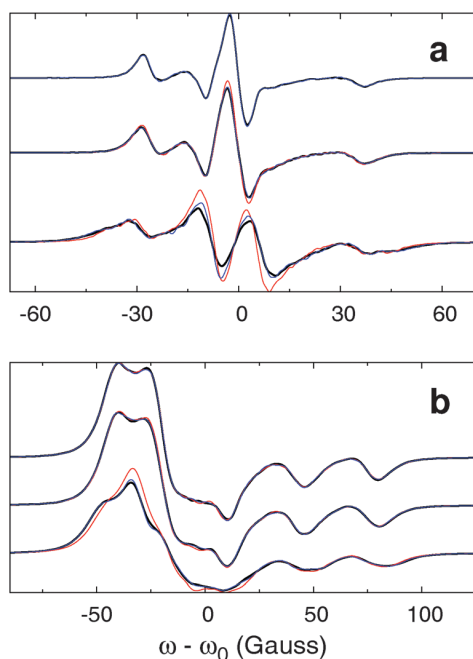


**Fig. 8** Comparison of the exact simulations in Fig. 5 (thick black), and the approximations of weak dipolar coupling (red) and separable matrices (blue). The latter approximation is consistently better than the former.

DNA(1,3). At the W-band, where the spectral lines are broader, the two approximations are seen to work well for DNA(1,4). The weak-coupling approximation fails for DNA(1,3) whereas the other approximation is still rather good.

Due to the significant speed-up achieved by the two approximate simulation schemes (11 min 38 s and 22 min 11 s, respectively, vs. 6 h 22 min for the exact treatment on a single 2.2 GHz CPU for the W-band spectra of DNA(1,5) in Fig. 8b) they offer an attractive alternative for the simulation of dipolar-broadened spectra from spin labels that are sufficiently far apart, and can be used for fast preliminary screening of the simulation parameters.

### C. Anisotropic tumbling with internal flexibility

Our final analysis is concerned with the influence of the stretching mode of the DNA helix on the cw-ESR spectra. For the illustrative purposes of the present study, the internal flexibility associated with stretching was modeled in a simplified manner as discussed in Section IIIC. The centers and widths of the Gaussian distributions in  $r_z$  are as given in the ‘avg.’ and ‘ $\sigma_z$ ’ columns of Table 1. To prevent large changes in the value of  $r_z$  during one integration time step with the chosen diffusion constants  $D_z = 0.25 \text{ \AA}^2 \text{ ns}^{-1}$  and  $D_z = 1 \text{ \AA}^2 \text{ ns}^{-1}$ , the value of  $h$  was reduced to 0.3 ns for both the X-band and W-band simulations. Trajectory lengths identical to the ones used for all other reported spectra were achieved by increasing the integration steps for a single trajectory, ‘stpN’, to 1000 and 300, respectively, at the X- and W-band (cf. Table 2). The other simulation parameters, including the components of the anisotropic diffusion tensor, were the same as the ones given in Table 2. The resulting spectra are shown in Fig. 9.

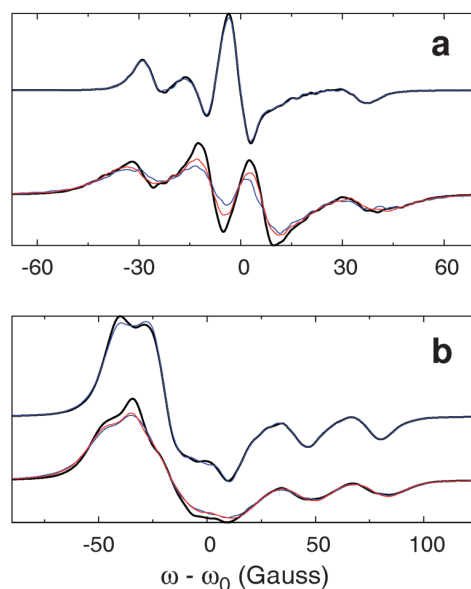


**Fig. 9** X-band (a) and W-band (b) spectra of DNA(1,4) (top) and DNA(1,3) (bottom) without (thick black) and with internal stretching dynamics using  $D_z = 0.25 \text{ \AA}^2 \text{ ns}^{-1}$  (thin blue) and  $D_z = 1 \text{ \AA}^2 \text{ ns}^{-1}$  (thin red).

From the figure, it is apparent that at the X-band the DNA(1,4) spectrum is not sensitive enough to reflect the presence of the modeled stretching dynamics with the assumed distribution width of  $\sigma_z = 3.2 \text{ \AA}$ . Although the spectrum shown at the top of Fig. 9a is for  $D_z = 0.25 \text{ \AA}^2 \text{ ns}^{-1}$ , increasing the time scale of the internal dynamics by a factor of four ( $D_z = 1 \text{ \AA}^2 \text{ ns}^{-1}$ ) resulted in an essentially identical spectrum (not shown). For the W-band spectrum of DNA(1,4) shown at the top of Fig. 9b, small differences between the spectra simulated without internal stretching dynamics and with  $D_z = 0.25 \text{ \AA}^2 \text{ ns}^{-1}$  are present in the lower-field,  $g_{xx}$  region of the spectrum. The deviations between the two spectra were even less visible for  $D_z = 1 \text{ \AA}^2 \text{ ns}^{-1}$  (not shown). In summary, we conclude that both X-band and W-band spectra of the DNA(1,4) system are not affected significantly by the presence of the assumed internal stretching dynamics.

In contrast, for DNA(1,3) both the X- and W-band spectra change substantially upon introducing the internal stretching motion on top of the global anisotropic tumbling. The dramatic differences between the spectra simulated without and with internal stretching using  $\sigma_z = 2 \text{ \AA}$  and  $D_z = 0.25 \text{ \AA}^2 \text{ ns}^{-1}$  suggested the possibility that one might be able to detect not only the presence of stretching fluctuations but also the time scale of these excursions. Indeed, as evidenced by the X-band spectra at the lower part of Fig. 9a, four times faster stretching dynamics ( $D_z = 1 \text{ \AA}^2 \text{ ns}^{-1}$ ) resulted in a spectrum significantly different than both other spectra. The W-band spectrum, on the other hand, appears not to allow access to the time scale of stretching, at least within the examined time window. Overall, the DNA(1,3) sample emerges as a promising candidate for probing local DNA dynamics.



## V. Conclusion

An efficient numerical integrator for the simulation of cw-ESR spectra of two dipolar-coupled nitroxides from trajectories was presented. By invoking the high-field approximation it was possible to reduce the computational effort of evolving the density matrix of the four coupled spins—two electron and two nuclear—by propagating only the sectors of the density matrix accessible to cw-ESR measurements. Nevertheless, the calculations were still a factor of  $\sim 50$  more costly than the simulation of the spectrum of a single nitroxide. To further reduce the simulation time, two approximate treatments of the dipolar evolution were considered. The first one—the approximation of weak dipolar coupling—is well known and routinely used in the simulation of DEER (PELDOR) time traces. The second approximation, based on projecting the full density matrix to the Hilbert spaces of the separate nitroxides after every step of dipolar evolution, appears to be novel. In the tests that were conducted we observed that the weak-coupling approximation worked only when the dipolar-coupling had almost no effect on the cw-ESR spectra (spin-label distance in the range of 20 Å). In contrast, the other approximation was perfect for distances down to 15 Å. When the separation was 10 Å, it produced a good W-band spectrum but failed at the X-band. Therefore, by employing the approximation proposed here, a factor of 20 speed-up can be achieved for spin-label separation of  $\geq 15$  Å. For shorter distances, the exact simulation has to be employed.

The developed simulation approach was used to explore whether 20 base-pair, double-helical, B-form DNA samples, containing two spin labels that bracket either one (DNA(1,3)) or two (DNA(1,4)) base pairs, can be used to access global and local DNA dynamics at room temperature. Our calculations of dipolar-broadened cw-ESR spectra for rigid DNA tumbling freely in solution indicated that a multifrequency study with such samples should be very informative about the anisotropic diffusion tensor of DNA. The spectra simulated by including idealized stretching dynamics suggested that using the DNA(1,3) sample it should be possible to detect differences in local DNA flexibility and dynamics due to, for example, different base-pair combinations bracketed between the two spin labels. Such studies with doubly-labeled DNA are expected to provide complementary information to the existing cw-ESR characterization of DNA dynamics from singly-labeled DNA samples.<sup>11–14,44,45</sup>

Modeling DNA stretching by a separate stochastic process that influences the spin label separation together with the anisotropic rotational diffusion of the whole molecule is intended to exemplify the virtually unlimited possibilities for including global and internal dynamics in a motional scheme like the one shown in Fig. 1. Such versatility results from the highly modular nature of the developed simulation approach based on stochastic trajectories of the motional models. The C++ routines used to simulate the reported spectra are freely available from the web page of the corresponding author.

Admittedly, here we have made no effort for complete modeling of the rich DNA dynamics, which in addition to stretching includes bending, twisting as well as coupling between the various modes. Generating trajectories of such

complex motions necessitates a coarse-grained but sufficiently realistic representation of DNA flexibility, the development and testing of which is a separate endeavor. The sensitivity of the multifrequency DNA(1,3) and DNA(1,4) spectra to such rich atomic-level motions, therefore, remains to be examined. There is no doubt, however, that the atomic-level information contained in such spectra will be subject to quantitative interpretation in the very near future. In fact, the computational investigation presented in this paper has provided a strong motivation to synthesize the doubly-labeled DNA samples with the purpose of performing the cw-ESR experiments that will test the theoretical predictions. The outcomes of this joint experimental–computational analysis will be reported in due course.

## Acknowledgements

We thank Dr Dominik Margraf for recording and kindly providing the X-band, room-temperature cw-ESR spectrum of DNA(1,5) shown in Fig. 4. D. S. is grateful to Prof. Thomas Prisner for his enthusiastic and multifaceted support of the reported work. The work of S. S. was supported by the Icelandic Research Fund (090026023).

## References

- 1 V. W. Cornish, D. R. Benson, C. A. Altenbach, K. Hideg, W. L. Hubbell and P. G. Schultz, *Proc. Natl. Acad. Sci. U. S. A.*, 1994, **91**, 2910.
- 2 A. Spaltenstein, B. H. Robinson and P. B. Hopkins, *J. Am. Chem. Soc.*, 1988, **110**, 1299.
- 3 T. R. Miller, S. C. Alley, A. W. Reese, M. S. Solomon, W. V. McCallister, C. Mailer, B. H. Robinson and P. B. Hopkins, *J. Am. Chem. Soc.*, 1995, **117**, 9377.
- 4 O. Schiemann, N. Piton, J. Plackmeyer, B. E. Bode, T. F. Prisner and J. W. Engels, *Nat. Protocols*, 2007, **2**, 904.
- 5 T. E. Edwards and S. T. Sigurdsson, *Nat. Protocols*, 2007, **2**, 1954.
- 6 P. Z. Qin, I. S. Haworth, Q. Cai, A. K. Kusnetzow, G. P. G. Grant, E. A. Price, G. Z. Sowa, A. Popova, B. Herreros and H. He, *Nat. Protocols*, 2007, **2**, 2354.
- 7 N. Barhate, P. Cekan, A. Massey and S. Sigurdsson, *Angew. Chem., Int. Ed.*, 2007, **119**, 2709.
- 8 W. L. Hubbell, A. Gross, R. Langen and M. A. Lietzow, *Curr. Opin. Struct. Biol.*, 1998, **8**, 649.
- 9 W. L. Hubbell, D. S. Cafiso and C. Altenbach, *Nat. Struct. Biol.*, 2000, **7**, 735.
- 10 L. Columbus and W. L. Hubbell, *Trends Biochem. Sci.*, 2002, **27**, 288.
- 11 B. H. Robinson, C. Mailer and G. Drobny, *Annu. Rev. Biophys. Biomol. Struct.*, 1997, **26**, 629.
- 12 T. M. Okonogi, A. W. Reese, S. C. Alley, P. B. Hopkins and B. H. Robinson, *Biophys. J.*, 1999, **77**, 3256.
- 13 T. M. Okonogi, S. C. Alley, A. W. Reese, P. B. Hopkins and B. H. Robinson, *Biophys. J.*, 2000, **78**, 2560.
- 14 T. M. Okonogi, S. C. Alley, A. W. Reese, P. B. Hopkins and B. H. Robinson, *Biophys. J.*, 2002, **83**, 3446.
- 15 P. Cekan, A. L. Smith, N. Barhate, B. H. Robinson and S. T. Sigurdsson, *Nucleic Acids Res.*, 2008, **36**, 5946.
- 16 X. Zhang, P. Cekan, S. T. Sigurdsson and P. Z. Qin, *Methods Enzymol.*, 2009, **469**, 303.
- 17 I. Krstić, O. Frolow, D. Sezer, B. Endeward, J. E. Weigand, B. Suess, J. W. Engels and T. F. Prisner, *J. Am. Chem. Soc.*, 2010, **132**, 1454.
- 18 P. P. Borbat and J. H. Freed, *Methods Enzymol.*, 2007, **423**, 52.
- 19 O. Schiemann and T. F. Prisner, *Q. Rev. Biophys.*, 2007, **40**, 1.
- 20 G. Jeschke and Y. Polyhach, *Phys. Chem. Chem. Phys.*, 2007, **9**, 1895.



- 21 Y. D. Tsvetkov, A. D. Milov and A. G. Maryasov, *Russ. Chem. Rev. (Engl. Transl.)*, 2008, **77**, 487.
- 22 J. Voss, L. Salwiński, H. R. Kaback and W. L. Hubbell, *Proc. Natl. Acad. Sci. U. S. A.*, 1995, **92**, 12295.
- 23 J. Voss, W. L. Hubbell and H. R. Kaback, *Proc. Natl. Acad. Sci. U. S. A.*, 1995, **92**, 12300.
- 24 M. Persson, J. R. Harbridge, P. H. R. Mitri, L.-G. Mårtensson, U. Carlsson, G. R. Eaton and S. S. Eaton, *Biophys. J.*, 2001, **80**, 2886.
- 25 E. Perozo, D. M. Cortes and L. G. Cuello, *Nat. Struct. Mol. Biol.*, 1998, **5**, 459.
- 26 E. Perozo, D. Marien Cortes and L. G. Cuello, *Science*, 1999, **285**, 73.
- 27 E. Perozo, A. Kloda, D. M. Cortes and B. Martinac, *Nat. Struct. Mol. Biol.*, 2002, **9**, 696.
- 28 E. Perozo, D. M. Cortes, P. Sompornpisut, A. Kloda and B. Martinac, *Nature*, 2002, **418**, 942.
- 29 G. Jeschke, V. Chechik, P. Ionita, A. Godt, H. Zimmermann, J. Banham, C. Timmel, D. Hilger and H. Jung, *Appl. Magn. Reson.*, 2006, **30**, 473.
- 30 E. J. Hustedt and A. H. Beth, *Annu. Rev. Biophys. Biomol. Struct.*, 1999, **28**, 129.
- 31 E. J. Hustedt, A. I. Smirnov, C. F. Laub, C. E. Cobb and A. H. Beth, *Biophys. J.*, 1997, **72**, 1861.
- 32 E. J. Hustedt, R. A. Stein, L. Sethaphong, S. Brandon, Z. Zhou and S. C. DeSensi, *Biophys. J.*, 2006, **90**, 340.
- 33 D. Sezer, J. H. Freed and B. Roux, *J. Chem. Phys.*, 2008, **128**, 165106.
- 34 E. Meirovitch, A. Nayeem and J. H. Freed, *J. Phys. Chem.*, 1984, **88**, 3454.
- 35 A. Polimeno and J. H. Freed, *J. Phys. Chem.*, 1995, **99**, 10995.
- 36 D. Sezer, J. H. Freed and B. Roux, *J. Phys. Chem. B*, 2008, **112**, 5755.
- 37 D. Sezer, J. H. Freed and B. Roux, *J. Phys. Chem. B*, 2008, **112**, 11014.
- 38 D. Sezer, J. H. Freed and B. Roux, *J. Am. Chem. Soc.*, 2009, **131**, 2597.
- 39 O. Schiemann, P. Cekan, D. Margraf, T. Prisner and S. Sigurdsson, *Angew. Chem., Int. Ed.*, 2009, **48**, 3292.
- 40 A. Marko, D. Margraf, P. Cekan, S. T. Sigurdsson, O. Schiemann and T. F. Prisner, *Phys. Rev. E: Stat. Phys., Plasmas, Fluids, Relat. Interdiscip. Top.*, 2010, **81**, 021911.
- 41 A. Abragam, *The Principles of Nuclear Magnetism*, Oxford University Press, New York, 1961.
- 42 S. Alexander, *J. Chem. Phys.*, 1962, **37**, 974.
- 43 A. Ponti, *J. Magn. Reson.*, 1999, **138**, 288.
- 44 E. J. Hustedt, A. Spaltenstein, J. J. Kirchner, P. B. Hopkins and B. H. Robinson, *Biochemistry*, 1993, **32**, 1774.
- 45 E. J. Hustedt, J. J. Kirchner, A. Spaltenstein, P. B. Hopkins and B. H. Robinson, *Biochemistry*, 1995, **34**, 4369.